Article

Slip Risk Prediction Using Intelligent Insoles and a Slip Simulator

Shou Xu [1], Md Javed Imtiaze Khan [1], Meysam Khaleghian [2,*] and Anahita Emami [1,*]

1   Ingram School of Engineering, Texas State University, San Marcos, TX 78666, USA; uzr14@txstate.edu (S.X.); m_k352@txstate.edu (M.J.I.K.)
2   Department of Engineering Technology, Texas State University, San Marcos, TX 78666, USA
*   Correspondence: khaleghian@txstate.edu (M.K.); a.emami@txstate.edu (A.E.)

Abstract: Slip and fall accidents are the leading cause of injuries for all ages, and for fatal injuries in adults over 65 years. Various factors, such as floor surface conditions and contaminants, shoe tread patterns, and gait behavior, affect the slip risk. Moreover, the friction between the shoe outsoles and the floor continuously changes as their surfaces undergo normal wear over time. However, continuous assessment of slip resistance is very challenging with conventional measurement techniques. This study addresses this challenge by introducing a novel approach that combines sensor fusion technology and machine learning techniques to create intelligent insoles designed for fall risk prediction. In addition, a state-of-the-art slip simulator, capable of mimicking the foot's motion during a slip, was developed and utilized for the assessment of slipperiness between various shoes and floor surfaces. Data acquisition involved the collection of pressure data and three-axial accelerations using instrumented shoe insoles, complemented by friction coefficient measurements via the slip simulator. The collected dataset includes four types of shoes, three floor surfaces, and four surface conditions, including dry, wet, soapy, and oily. After preprocessing of the collected dataset, the simulator was used to train five different machine learning algorithms for slip risk classification. The trained algorithms provided promising results for slip risk prediction for different conditions, offering the potential to be employed in real-time slip risk prediction and safety enhancement.

Keywords: intelligent insole; fall risk prediction; slip simulator; sensor fusion; machine learning

1. Introduction

A slip-and-fall mishap happens when an individual's footing falters, leading to a tumble to the ground caused by a slip, trip, or misstep. These incidents are not confined to specific locales; rather, they can transpire anywhere, with a pronounced propensity for occurrence on damp or slick surfaces found in bathrooms, kitchens, and outdoor spaces. Furthermore, these accidents may arise due to uneven terrains, inadequate lighting, or obstructions along pathways. Notably, statistics from the U.S. Bureau reveal that in 2020 alone, there were 31.4 instances of nonfatal falls, slips, and trips for every 10,000 full-time employees [1]. These slip-and-fall episodes take the lead in generating workers' compensation claims within the construction sector [2]. Among unintentional injuries and fatalities, falls attributed to slipping rank as the second most frequent cause, second only to vehicular accidents [3]. Cognizant of the prevailing circumstances, two predominant kinds of falls emerge as trips and slips. A trip involves a disruption in the natural course of the swinging leg, culminating in a dislocation of the center of gravity from its support base and, in turn, leading to a fall. Conversely, a slip stems from the insufficiency of friction between the walking surface and an individual's footwear, thus inducing imbalance and eventual descent. In establishing a safe threshold of traction during walking, it is widely acknowledged that a coefficient of friction (COF) surpassing 0.20 is imperative for flat surfaces [4]. It is important to note, however, that this requisite COF value may fluctuate based on age and impairments, serving as a means of ensuring safer ambulation [5,6].

Given the site-specific variables that influence slip resistance, regular assessment of floor surface slipperiness proves indispensable [7–9].

To gauge the extent of slip resistance between footwear and flooring, tools designed to measure friction have been developed. Despite these instruments collectively harnessing the principle of friction to gauge slip resistance, substantial divergences persist in the measurement methodologies adopted by distinct slipmeters [10,11]. In general, these slipmeters can be categorized into two main groups: human-based and machine-based [12]. Human-based slipmeters hinge on the engagement of human participants to measure friction, and tend to be characterized by larger dimensions. In contrast, machine-based counterparts exhibit portability and depend on the measurement of human gait parameters, a metric solidified through the rigorous biomechanical examination of human locomotion [12]. The quantitative prerequisites for slip incidents, encompassing normal force build-up rate, contact pressure, sliding velocity, and computation time, have been subjected to exhaustive scrutiny and validation [13].

The instrumented insole emerges as a proficient technique for capturing an extensive spectrum of gait data, spanning from tap dance to even the intricacies of golf-swing analysis [14]. In the nascent phases of its development, dating back to the 1990s, devices were meticulously engineered to measure the distribution of pressure beneath the foot, harnessing the capabilities of force-sensitive resistors (FSRs). These devices played the role of quantitatively evaluating the distinctions between shuffling and walking gait patterns [14,15]. Early reviews by Abdul et al. (2012) [16] and Tan et al. (2015) [17,18] summarized the various solutions presented by researchers to measure foot plantar pressure using in-shoe system for diagnosing lower limb problems, footwear design, sport biomechanics, injury prevention, and other applications. Over the last five years, more advanced studies pertaining to instrumented insole have been made concerning various aspects, such as improvement in sensor technologies [19–22], development of insole-integrated sensing devices, and human movement classification [23–27], which are mainly used in clinical settings including post-surgery biomechanical assessment, intra-operative assessment, orthotics design, and laboratories to understand the mechanisms governing human gait and posture [28].

With regard to applications, many researchers have focused on the assessment of different gait parameters, particularly concerning the center of pressure path (COPP). Based on these results, studies have been conducted to classify human gait for identification and fall detection using artificial intelligence algorithms. However, not only diseases, but the shoes (sole material, pattern), the nature of the road surface, and contaminations on the road surface can cause gait disturbances. Thus, evaluating the interaction and slipperiness between shoes and surfaces is essential to assess slip incident/fall risk.

Surprisingly, there exists a need for research findings that establish a correlation between slipmeter-measured slipperiness and the corresponding gait pattern on a given surface. In order to fill this gap, a technique for real-time slip risk prediction and classification was developed based on the correlation matrix of extracted gait feature parameters and the coefficient of friction in this study. We aim to predict the slip risk under different conditions using data collected using custom-made instrumented insoles with embedded force-sensitive sensors and a three-axis accelerometer. A laboratory-type machine-based slip simulator, capable of applying a wide range of normal pressures at varying ankle angles, was designed and constructed.

2. Methodology

2.1. Portable Slip Simulator

A laboratory-type machine-based slip simulator, depicted in Figure 1, was employed to quantify the coefficient of friction (COF) for different shoe–floor configurations. The slip simulator encompasses a vertical actuator as well as a horizontal actuator, both instrumental in effectuating the movement of the footwear sample across the test surface. The vertical force can be applied with a magnitude of up to 700 N, while its velocity ranges from 0 to

a maximum of 1 m/s. In parallel, the horizontal force can be exerted up to 400 N and at velocities spanning from 0 to 0.50 m/s.
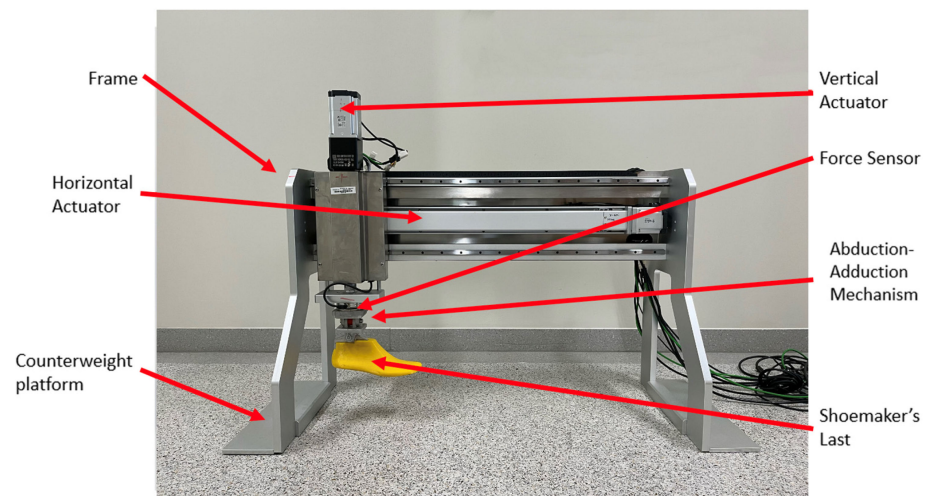

Figure 1. Laboratory-type machine-based slip simulator measuring COF.

An ankle mechanism is affixed to the lower terminus of the vertical actuator. This mechanism serves to suspend the shoe sample, adhering to standardized dimensions, via a 3D-printed shoemaker's last. As shown in Figure 2, the ankle mechanism with a mechanically adjustable joint allows a simultaneous manipulation of plantar flexion–dorsiflexion, abduction–adduction, and inversion–eversion angles. The forces generated during the experiment were captured by a six-axis force/torque transducer (ATI Industrial Automation AXIA80–M20) positioned between the ankle mechanism and the vertical actuator.
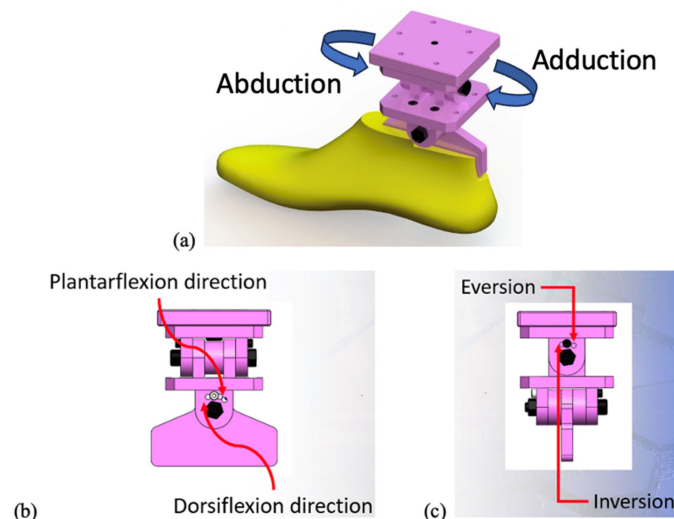

Figure 2. CAD Model of the ankle mechanism (**a**) Ankle mechanism attached to the 3D-printed shoemaker's last, (**b**) direction of screw hole for making plantar flexion and dorsiflexion angle, and (**c**) component required for making abduction and adduction angle.

Operational control of the apparatus, including motion and pertinent parameters, was achieved through the employment of Pro-motion@ (Version 5.06), supplied by the actuator manufacturer (E-motion America, Inc., Temecula, CA, USA). This software is integrated within the Microsoft Windows 10 operating environment. Furthermore, signals emanating from the force/torque transducer were meticulously collected via the proprietary Java program furnished by the manufacturer (E-motion America, Inc.). These signals were subsequently documented onto the host computer via an Ethernet connection, operating at a sampling frequency of up to 8 kHz.

The 230 V electrical power connection is required to run the machine. The machine structure is made of aluminum 6061 alloy, and the overall dimensions are 1412 × 500 × 945 mm (length × width × height). The gross weight of it is 175 lbs., but additional dead loads can be applied to the structure if required for experimental stability.

2.2. Instrumented Insole

A pair of custom insoles were 3D printed using TPU filament with an Atomstack Cambrian Pro. printer (Atomstack Technologies Co., Ltd. Shenzhen, China). Each insole was instrumented by five FSRs (FlexiForce A301 25, manufactured by Tekscan, Inc. Norwood, MA, USA) and a triple-axis accelerometer (ADXL335—5 V (±3 g analog out) manufactured by Analog Devices, Inc. Wilmington, MA, USA). Two FSRs were at the forefoot and three were at the posterior regions (see Figure 3) to achieve the pressure mapping during different walking environments. The thickness of the FSR is 0.23 mm, and double-sided tape (300LSE series 9495LE double-sided PET tape manufactured by 3M. (3M Center, MN, USA) was used to attach the FSR to the insole, as recommended by the FSR manufacturer, to avoid unwanted cushioning restricting sensitivity. The 3D-printed load concentrator (or puck) was fitted on top of the sensitive area of the FSR with caution, as this reduces the chances of applying lateral forces to it. The accelerometer was placed at the midfoot region. A FlexiForce Quickstart Board (QSB) (Tekscan, Inc. Norwood, MA, USA) open-amp circuit board was used with each FSR to power and obtain a signal. FSRs were designed to show 0.50 V at zero load conditions and reach a max 5 V out at 25 lbs.
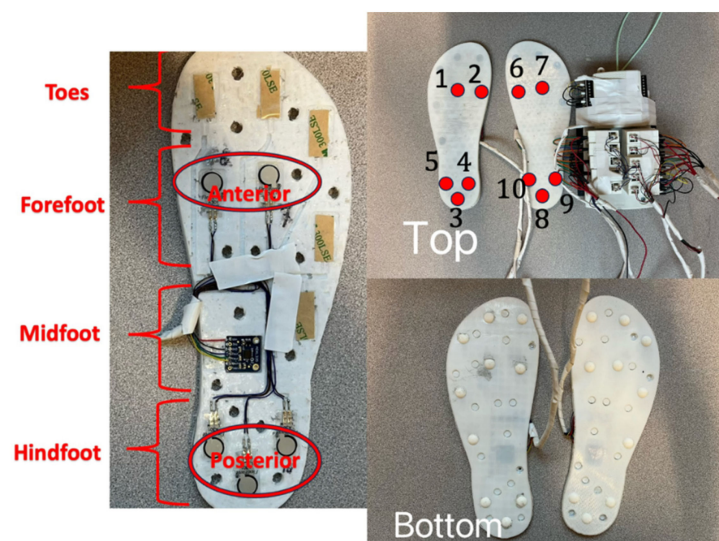

Figure 3. 3D-printed instrumented insole with FSRs locations of US 9.5 men's foot size.

Wires carrying signals from the QSB and accelerometer were connected to the host computer via National Instrument's USB-6218 DAQ system (National Instruments Corp. Austin, TX, USA). A LabView program collected the signals at 1000 Hz during the experiment. DC 9 V power was supplied to the QSB and DC 3 V power for the accelerometer using an AC adapter to reduce the voltage fluctuation and noise to the system.

All of the FSRs and QSBs were made as a pair for installation into the insole and calibration. A compressive load of 25 lbs was applied by a universal testing machine before use in the experiment. According to the manufacturer's instructions, the 6-point calibration test was performed, and all of the pairs showed an aligned increment in sensitivity with the applied load. The R^2 values were above 0.985, on average, for each pair.

2.3. Design of Experiment

The assessment of the COF encompassed the utilization of four distinct footwear variants, labeled as Types A, B, C, and D. Moreover, the study incorporated three distinct floor materials, cemented, mosaic, and concrete. To account for real-world scenarios,

four different contamination conditions were introduced, including no contamination, watery substances, soapy water, and kitchen oil (see Figure 4). The rationale behind this multifaceted approach was to scrutinize the interplay of various factors on slip resistance. Notably, the performance of the same shoe exhibited variations in response to the diverse factors, highlighting the nuanced nature of slip resistance. To ensure the integrity of the findings, all of the experimental tests were consistently conducted in a uniform direction of operation and maintained uniform boundary conditions. This meticulous approach was adopted to eliminate potential biases that could arise from varying experimental setups.
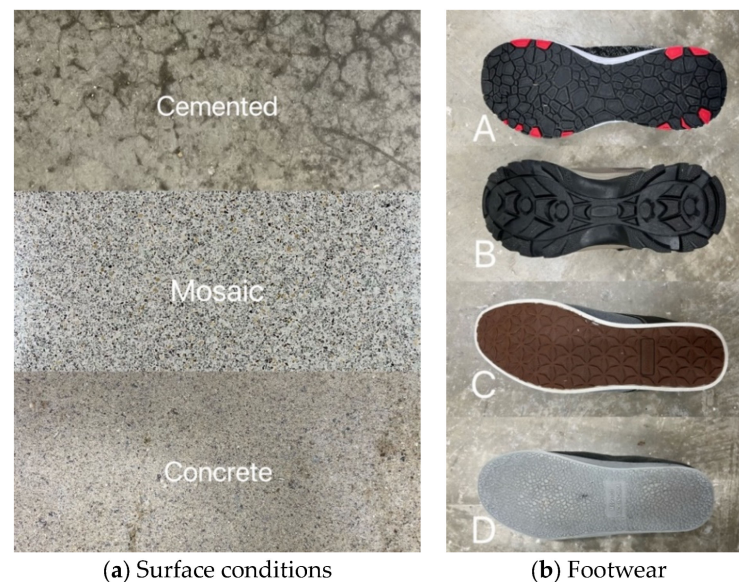

(**a**) Surface conditions   (**b**) Footwear

Figure 4. Surface conditions and footwear samples of Type A, B, C, D used in experiments.

In the context of the instrumented shoe insole, the experimental setup closely mirrored that of the slip simulator. Subsequently, the outcomes derived from these insole experiments were employed to establish a correlation with the COF measurements obtained from the slip simulator under equivalent conditions. This correlation aimed to discern the relationship between the readings of the slip simulator's COF and the data gathered through the instrumented insole experiments.

The categorization of friction levels, as determined by the slip simulator, is outlined as follows in Table 1:

Table 1. Slip risk level based on COF.

Range of COF	Slip Risk
$0.4 < \text{COF}$	Low
$0.2 < \text{COF} < 0.4$	Medium
$\text{COF} < 0.2$	High

3. Experiment Results

3.1. Measurement of COF by the Slip Simulator

The predetermined reference value for the vertical actuator's normal force was set at 100 N, with a slight variation ranging from 110 N to 95 N, equating to approximately 15%. The coefficient of friction (COF) serves as a quantification of the frictional force (F_H) relative to the normal or vertical force (F_V) exerted on the foot. Mathematically, the COF is defined as $\mu = F_H/F_V$. During the experimental procedures, the frictional force was collected from the force/torque sensor, with the specific value contingent on the normal load imposed by the vertical actuator. Taking walking shoes (Type B) on a mosaic surface as an example, Figure 5 graphically illustrates the COF in both dry and oil-contaminated conditions. The calculation of the coefficient of friction (COF) was conducted while maintaining the normal

force at a constant value. Computation extended for a duration of 600 ms, with a frequency of 100 Hz, commencing after the attainment of the prescribed normal force.
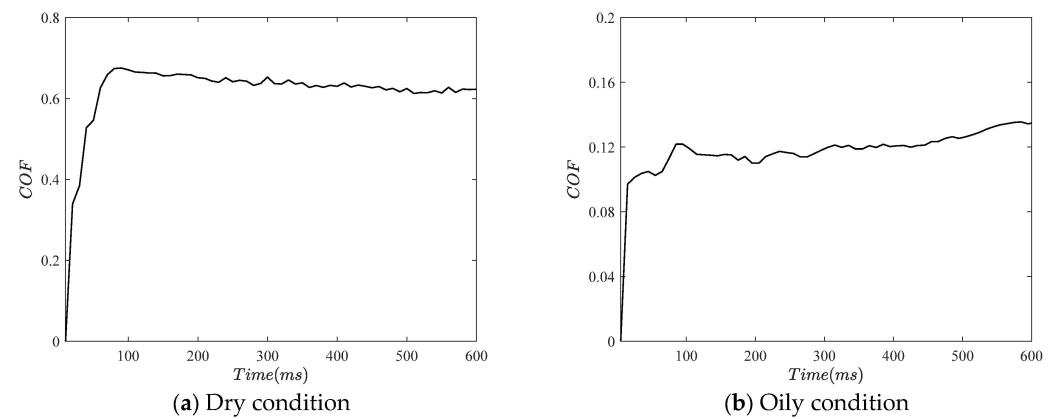

(**a**) Dry condition　　　　　　　　　　　(**b**) Oily condition

Figure 5. COF of the walking shoe on the mosaic floor.

To uphold the reproducibility of the system, the identical shoe was tested at least four times under consistent experimental conditions. The standard deviation observed for both the normal force and the frictional force ranged from 1 to 3 N, affirming the system's reliability. The graphical representation of the COF for different floorings and contamination levels obtained from the experiment is presented in Figure 6 as a bar chart. In scenarios devoid of oil contamination, the friction coefficient of Type A (Type A) surpassed the threshold of 0.40 on all three surface types. However, in the presence of oil on varying surfaces, the friction coefficient for the walking shoes diminished significantly, reaching a high-risk level in terms of slip potential.
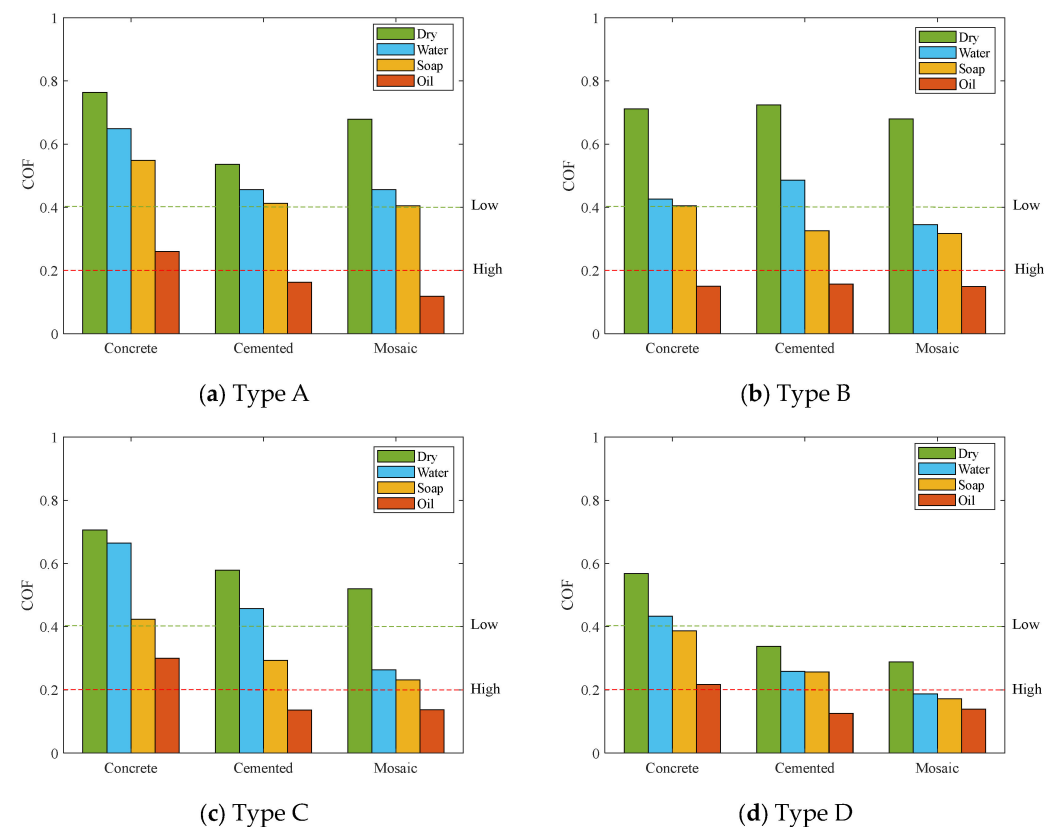

(**a**) Type A　　　　　　　　　　　　　(**b**) Type B

(**c**) Type C　　　　　　　　　　　　　(**d**) Type D

Figure 6. COFs for different floor and contamination conditions measured by the slip simulator.

3.2. Gait Data from the Instrumented Insole

To attain more accurate and comprehensive gait insights, the instrumented insole experiment was meticulously replicated six times under identical experimental conditions. This iterative approach allowed us to capture a broader range of foot pressure maps and acceleration signatures. Notably, the gait signature exhibited notable variations between the slip-resistant and slippery conditions.

Considering the safety shoes on a mosaic surface, Figure 7 shows cases of the foot pressure distribution measured by the instrumented insole for both legs. Figure 7a corresponds to a high-friction surface (safety shoes on a dry mosaic floor), while Figure 7b represents a slippery surface (safety shoes on an oily mosaic floor). The temporal and spatial dimensions were contingent on the number of steps taken by the human subjects, ensuring an accurate portrayal of natural walking patterns.
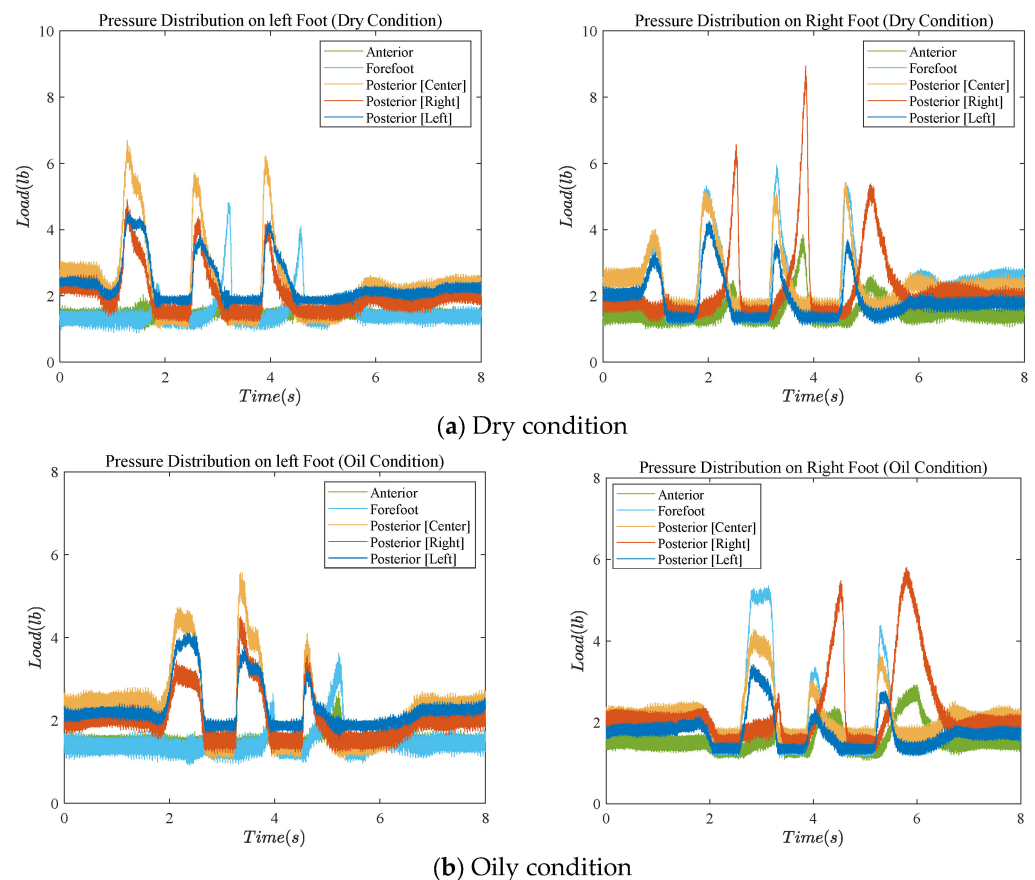

(**a**) Dry condition

(**b**) Oily condition

Figure 7. Foot pressure map of the Type A shoes while walking on the mosaic surface.

Broadly, on the high-friction surfaces, a greater number of strides were observed within a given time frame compared to the slippery surfaces, resulting in a shorter swing phase duration. This phenomenon is indicative of the enhanced stability provided by high-friction surfaces.

The foot pressure distribution further accentuated these distinctions. On slip-resistant surfaces, there was a noticeable pressure differential from heel to toe, with posterior (center and right side) peak pressures being higher. This indicated a more pronounced toe-off angle during walking on dry surfaces. Conversely, on the oily mosaic floor, the peak pressure difference across all five zones decreased, indicating a relatively more uniform pressure distribution on the foot during walking.

The depiction of foot acceleration '*g*' during gait on a mosaic surface, specifically with safety shoes on both the dry and oil-contaminated surfaces, is illustrated in Figure 8. In this portrayal, a_x corresponds to horizontal acceleration, a_y to lateral acceleration, and a_z

to vertical acceleration. The presented acceleration data effectively corroborate the stride patterns inferred from the pressure information. Across the high-friction surface, notable fluctuations in a_z and a_x are observed, primarily attributed to the leg's swing motion. Conversely, a_y exhibits relatively modest fluctuations in gravitational force (g) values in the high-friction scenario. However, in instances where surface friction diminishes, a distinct trend emerges: the overall acceleration decreases, influenced by the reduced stride length. The interaction between foot acceleration and friction provides valuable insights into the intricate relationship between gait dynamics and surface conditions, further reinforcing the significance of slip-resistant measures.
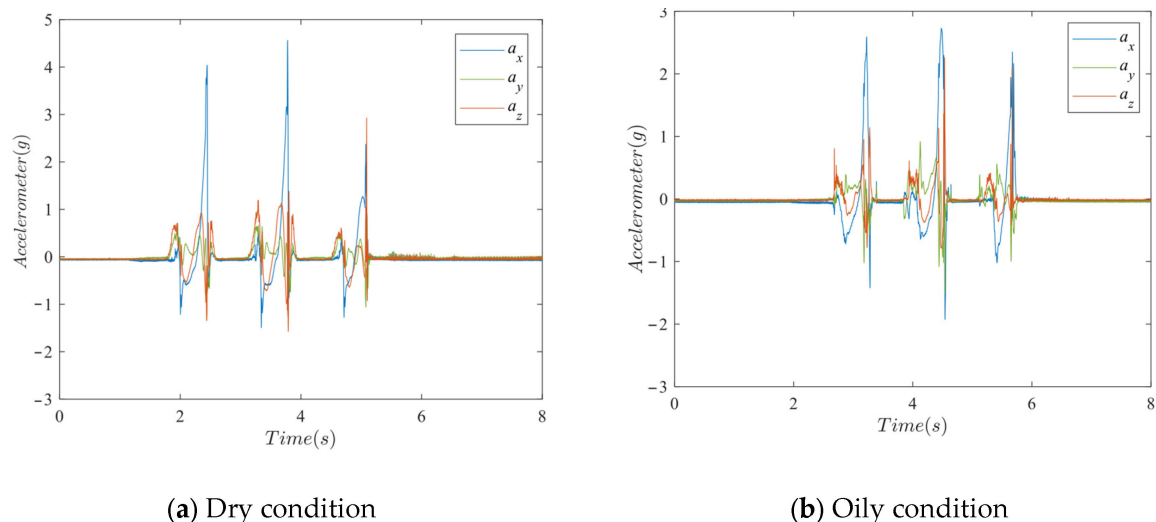

(**a**) Dry condition　　　　　　　　　　　　　　　(**b**) Oily condition

Figure 8. Acceleration map of type A shoes during the walk on the mosaic surface.

Figure 9 presents comparison of the power spectrum density (PSD) of the acceleration data acquired during walking on a mosaic surface with safety shoes under both dry and oily conditions.

Furthermore, changes in the walking surface and conditions induce notable fluctuations in the frequency spectrum. For example, walking on a low-friction surface (oil-contaminated surface) yields diminished local magnitude (8–12 Hz) in the x direction compared to the scenario with higher friction (dry surface), although the highest magnitude levels remain relatively close. In the z direction, compared with the high friction case, the PSD magnitude of the low friction case decreases significantly at 1–6 Hz.

It is also noted that there are considerable differences in signals at high frequencies (between 100 and 200 Hz), as shown in Figure 10. At these frequencies, variations are more noticeable. Using Figure 10a as an example, as high friction conditions can result in more energy dissipation in the system, leading to higher amplitude vibrations at certain frequencies, particularly in the 100–200 Hz range. Meanwhile, low friction conditions may result in more cautious motion, leading to fewer high-frequency components in the acceleration signals. Therefore, the power calculation helps quantify the energy content in the signal, making it easier to compare and correlate with the friction coefficient. The varying effects on the PSD when different types of shoes encounter oil surfaces can be observed in Figure 10b. Some shoes are specifically designed or made from materials that perform better in such conditions, resulting in a more significant drop in the PSD, which indicates lower vibrations generated during contact.
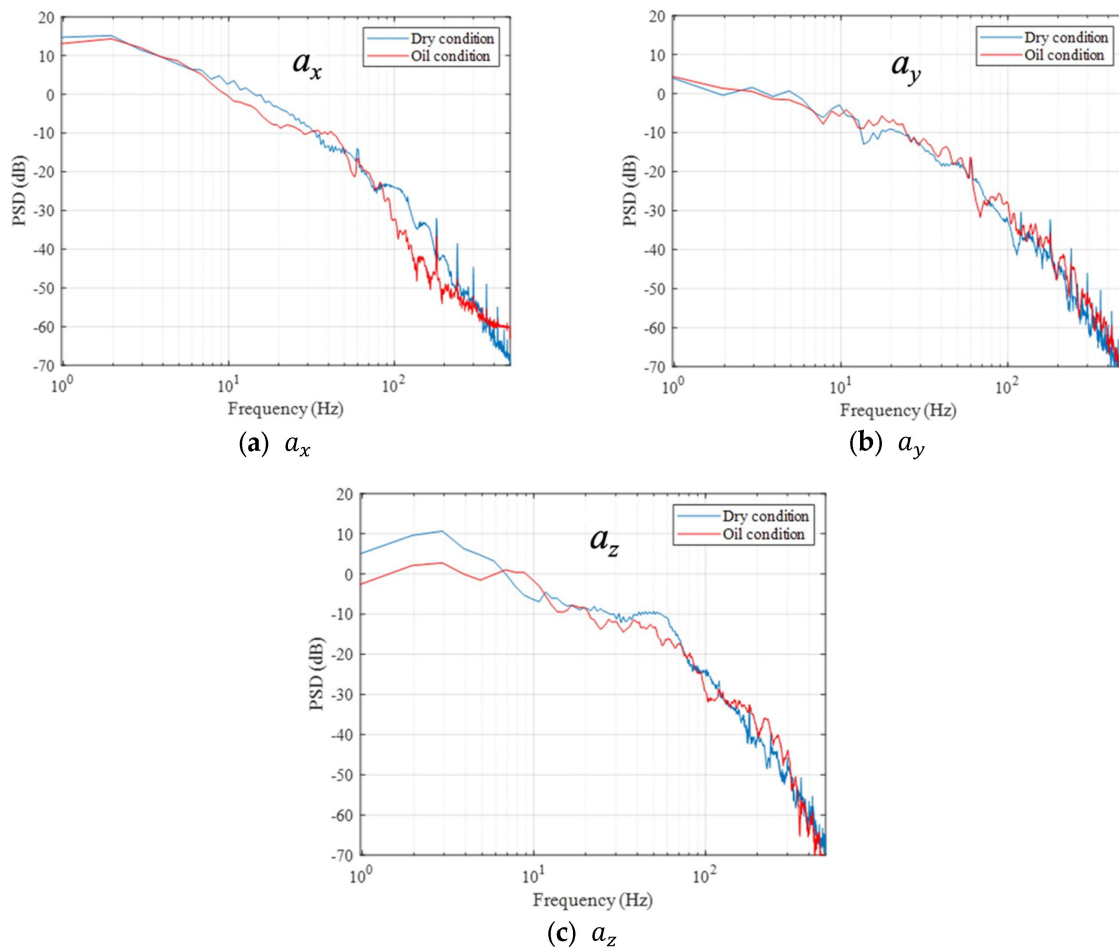
(**a**) a_x

(**b**) a_y

(**c**) a_z

Figure 9. Power spectrum density during the walk on mosaic surface with Type A shoes.
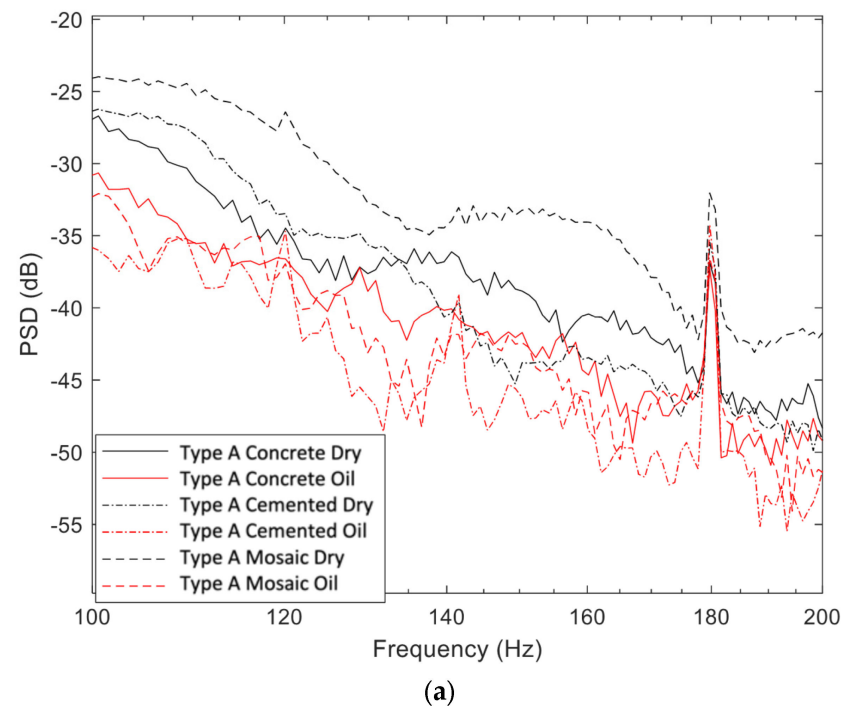

(**a**)

Figure 10. *Cont.*
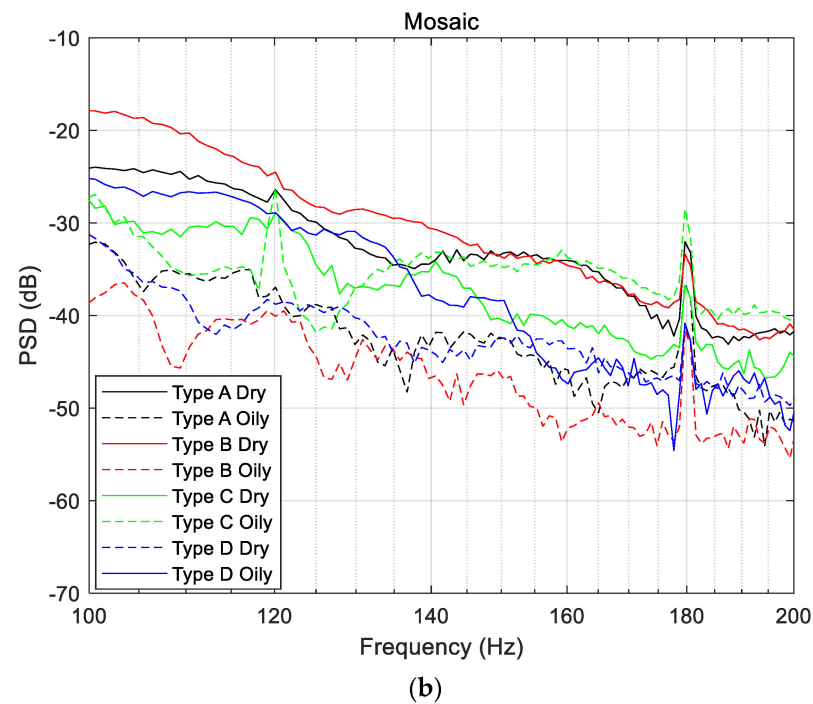
(b)

Figure 10. Power spectrum density of a_x during the walks (**a**) on multiple surfaces with Type A shoes in dry and oil conditions, and (**b**) on mosaic surface with all types of shoes in dry and oil conditions.

This comprehensive spectral analysis deepens our understanding of the intricate interplay between gait dynamics and surface conditions, underscoring the dynamic nature of human locomotion and the role of friction in shaping these patterns.

4. Correlation between Insole Data and Coefficient of Friction

4.1. Gait Features Recognition

We studied human gait by analyzing the pressure and acceleration signals collected from the instrumented insoles. Analysis of the acceleration signals over time unraveled the stride duration.

Concurrently, the pressure signals provide additional insights into the distribution of weight over the foot during walking. It furnished an array of features, encompassing pressure peaks and peak-to-peak lengths for each individual force-sensitive resistor (FSR) on both feet. Moreover, changes in the center of pressure point (Yc) throughout the walking cycle provide insights into how the human subjects adapted their foot motion and pressure zones to ensure safe walking. The calculation of the center of pressure point for each foot was accomplished through the following formula:

$$Y_c = \frac{\sum_{i=1}^{5} P_i y_i}{\sum_{i=1}^{5} P_i} \tag{1}$$

where P signifies pressure, and y represents the distance between the FSR and the heel point.

From the data achieved through the instrumented insole experiments, a total of fifteen features were extracted from the pressure signals. These encompassed force peaks at distinct measurement points (e.g., F_{1max}, F_{2max}, F_{3max}, F_{4max}, F_{5max}, F_{6max}, F_{7max}, F_{8max}, F_{9max}, F_{10max}), as well as mean and peak values of the center of pressure points for both the left and right feet (e.g., $\overline{Y}_{cL}$, $\overline{Y}_{cR}$, Y_{cLp}, and Y_{cRp}). The temporal dynamics of a gait cycle were also encapsulated through the feature t_{GC} = Time for Gait Cycle, a metric derived from the ten measured forces of the left and right feet. It is determined from the curves of ten measured forces from the left and right feet, and is equal to the average peak-to-peak length between force peaks at each measurement point.

Furthermore, the most important three characteristics are extracted from the acceleration signals, including the peak accelerations in the x, y, and z directions (e.g., a_{yp} and a_{zp}).

We analyzed these extracted features, leading to the development of a comprehensive correlation matrix, illustrated in Figure 10, which illustrates distinct relationships involving the coefficient of friction (COF), but with different dependent variables. In Figure 11a, taking a_{xp} as an example, it is positively correlated with the COF. a_{xp} values tend to increase as the COF increases. While we observe F_{9max}, as shown in Figure 11b, an inverse correlation can be seen between the COF and the pressure at the right heel. This indicates that the peak of the pressure at the right heel tends to decrease as the COF increases. If we connect the two relationships, it shows how changing the COF affects different physical parameters. For example, higher COF values lead to increasing acceleration peaks.
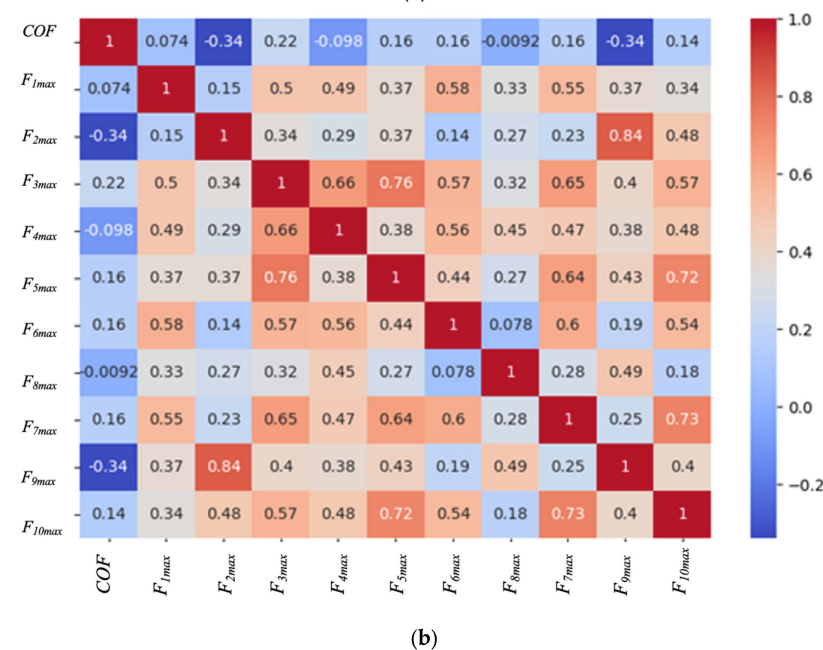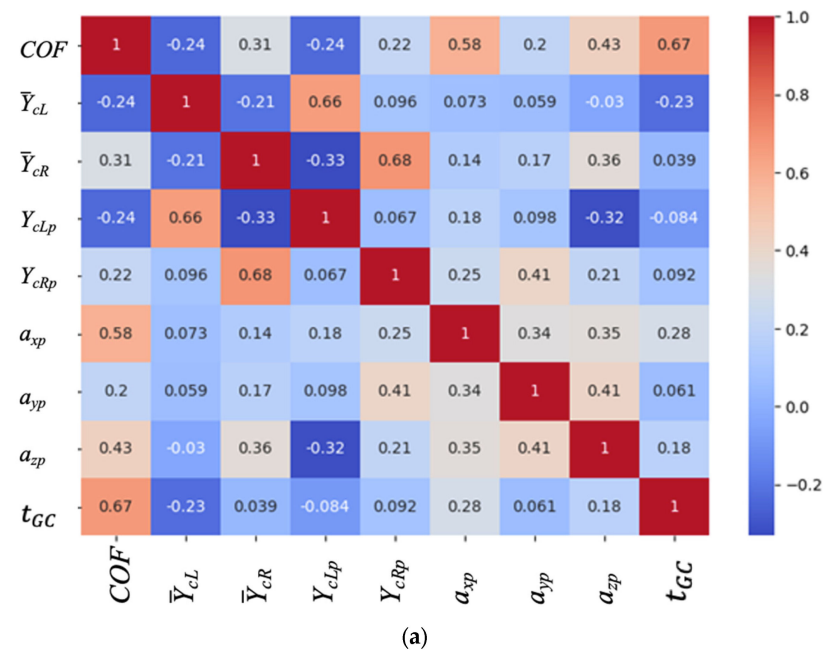

(a)

(b)

Figure 11. (**a**) Acceleration correlation of the gait features to the COF, and (**b**) force correlation of the gait features to the COF.

Therefore, this analysis unveiled intriguing insights, showcasing that certain gait features including $\overline{Y}_{cR}$, a_{xp} and t_{GC} exhibited a robust positive correlation with the COF. Conversely, F_{9max} has a slightly stronger negative correlation with the COF. Through this comprehensive analysis, we aimed to unravel the intricate interplay between gait dynamics and slip resistance, fostering a deeper understanding of the biomechanical nuances that influence human locomotion.

4.2. Data Preprocessing for Machine Learning Models

In order to achieve the best accuracy, the five strongly correlated parameters (F_{9max}, $\overline{Y}_{cR}$, a_{xp}, a_{zp}, t_{GC}) collected from the instrumented insole served as the machine learning inputs for the subsequent model assessment. The friction coefficient measured by the slip simulator was considered to determine the class label of the model. To facilitate classification, the slip risks were discreetly labeled as 'Low', 'Medium', and 'High'. There are 48 sets of strongly correlated parameters, which include four distinct footwear variants, three distinct floor materials, and four different contamination conditions. In the model for slip risk classification, 36 sets of parameters (75%) randomly selected from a total of 48 sets of strongly correlated parameters were used for model learning, and the remaining 12 sets (25%) were used for risk classification.

Prior to model input, we employed linear discriminant analysis (LDA) to reduce the dimensionality of the features, in order to enhance model performance. Then, the dataset was passed through several widely used algorithms, namely support vector machine (SVM), decision tree classifier (DT), random forest classifier (RF), k-nearest neighbor classifier (KNN), and linear regression (LR) classifier, to figure out the best-suited classification algorithm for this research. The grid search algorithm was applied to each classifier's model, and the pipeline fitting was for the SVM and LR models only.

The classification of the dataset by different classifiers is shown in Figure 12. The classifiers' performances are summarized in Table 2. Notably, RF and LR exhibited superior test accuracy, precision, recall, and F1 in comparison to the other algorithms. In addition, the KNN, RF, LR, and SVM classifiers demonstrated a commendable ability to correctly classify the majority of data points, with just one or two misclassifications. While DT achieved the primary goal of class label grouping, it did entail a few instances of misclassification. Among the classifiers considered, including the KNN, RF, LR, and DT classifiers, SVM exhibits superior learning precision and generalization abilities. Therefore, SVM can be more appropriate for real-time slip risk classification with very high slip risk classification accuracy, suggesting its suitability for applications in fall risk assessment. Through this comprehensive model assessment, we explored the potential of using the correlation between instrumented insole data and the coefficient of friction to predict slip risk.

Table 2. Performance of classifiers.

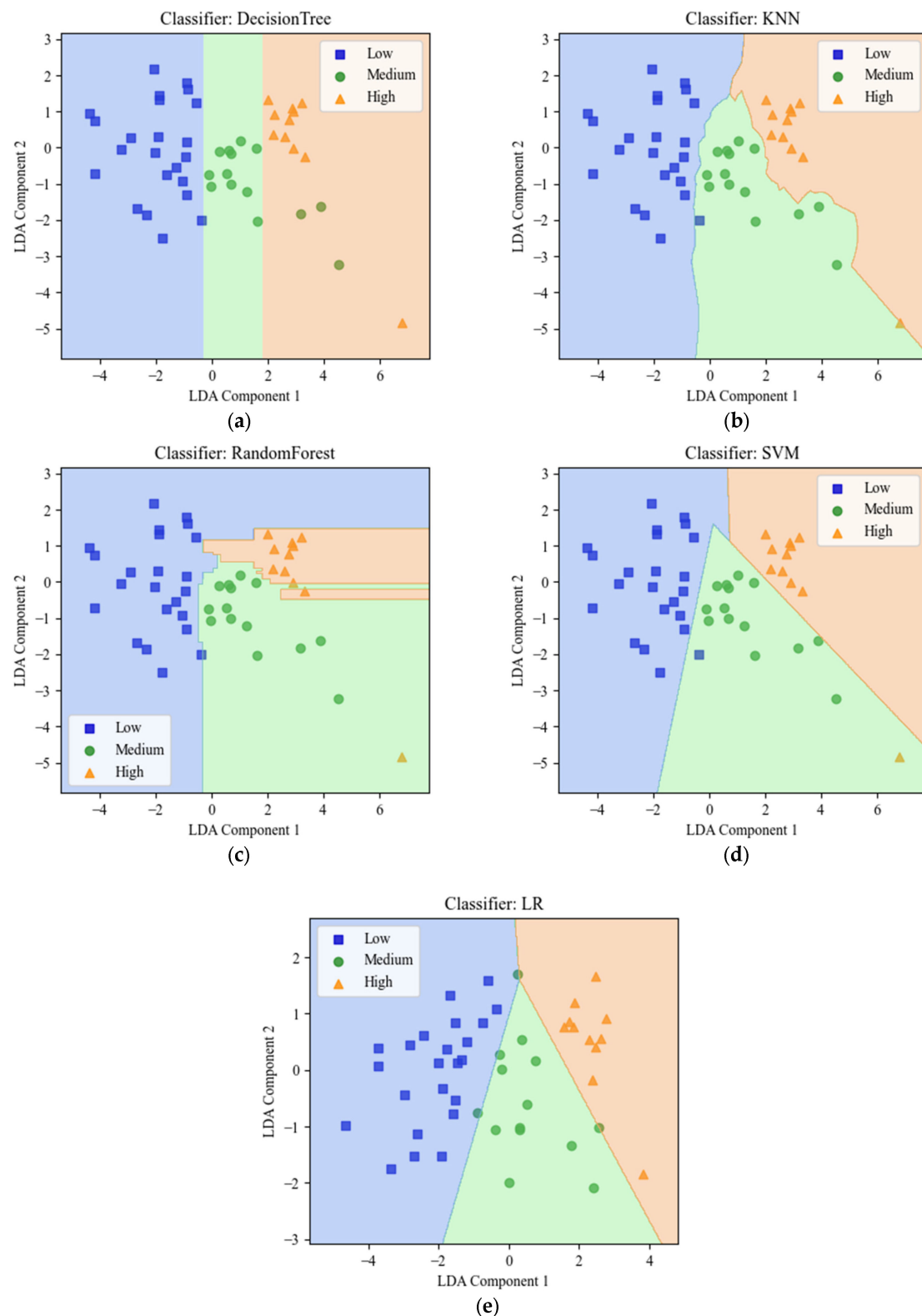| Classifier	Train Accuracy	Test Accuracy	Precision	Recall	F1
DT	97.2%	83.3%	86.7%	77.8%	75%
KNN	100%	83.3%	86.7%	83.3%	82%
RF	100%	91.7%	91.7%	88.9%	88.6%
SVM	100%	83.3%	86.7%	83.3%	82%
LR	97.2%	91.7%	95.8%	88.9%	91.1%

Figure 12. Performance of classifiers in a graphical way: (**a**) DT, (**b**) KNN, (**c**) RF, (**d**) SVM, and (**e**) LR.

Nevertheless, errors are unavoidable, owing to the noises and measurement errors. The sources of errors include ambient noises, as well as noises stemming from hardware (electronics), the DAQ system, wires, and connections to the DAQ system. More information on the sources of noise can be found in studies conducted by Yang et al. [29,30].

5. Conclusions

Evaluating the interaction and slipperiness between shoes and surfaces holds significant importance in the prevention of fall accidents and safety enhancement. Using smart insoles combined with machine learning, a cost-effective and accurate wearable solution has been developed for fall risk prediction. Notably, it delivers real-time, comprehensive gait data, rendering it a compelling alternative for slipperiness prediction compared to traditional slipmeters.

The primary objective of this research was two-fold: first, to engineer a slip simulator capable of simulating diverse ankle formations during walking; and second, to design an economical intelligent insole for real-time slip risk prediction. To achieve this research objective, measurements of the COF by the slip simulator for four shoe types under four different contamination conditions of three distinct floor materials were carried out. Based on the sensor signals collected from the instrumented insole, the effects of the slip-resistant and slippery conditions on foot pressure distribution, acceleration, and power spectrum density of the acceleration were analyzed. Furthermore, gait feature recognition was carried out, and five strongly correlated parameters with the COF were extracted as input parameters for the machine learning models. The value of the COF was used as the risk level classification, and the classification performance achieves high accuracy and precision. The study established a correlation between the coefficient of friction and gait parameters under a given combination of footwear variants, floor materials, and contamination conditions. The slip risk identification and classification technique presented in this study can be used for slip detection and slip risk assessment, as well as for the evaluation and design of footwear. On the other hand, the developed smart insole can be used as a medical monitoring device to monitor gait.

For future developments, there are opportunities for significant refinement. Methods of optimal sensor placement can leverage limited spatial positions to gather valuable information effectively. Future research could further enhance insole design by integrating sensor placement optimization techniques [31,32], enabling comprehensive monitoring of foot plantar pressure and distinguishing a wider array of gait types. The correlation of gait features with the COF and the performance of the classifier can be enhanced by amassing a larger corpus of data points, fostering a more robust predictive capability. Moreover, the connection infrastructure for the force-sensitive resistors and accelerometers could be substantially ameliorated through the introduction of a printed circuit board and a flexible ribbon connection. This measure not only bolsters accuracy, but also attenuates noise interference in the signal. Furthermore, the potential to optimize the 3D-printed insole's thickness holds promise for augmenting the response quality during experimental trials. By embarking on these future refinements, the research is poised to elevate its predictive capabilities and real-world applicability.

Author Contributions: Investigation, S.X. and M.J.I.K.; Data curation, S.X.; Writing—original draft, S.X. and M.J.I.K.; Writing—review & editing, S.X. and A.E; Supervision, M.K. and A.E.; Project administration, M.K. and A.E. All authors have read and agreed to the published version of the manuscript.

Conflicts of Interest: The authors declare no conflict of interest.

References

1. A Look at Falls, Slips, and Trips in the Construction Industry. The Economics Daily. Available online: https://www.bls.gov/opub/ted/2022/a-look-at-falls-slips-and-trips-in-the-construction-industry.htm (accessed on 22 February 2023).
2. Make Fall Safety a Top Priority. Available online: https://www.nsc.org/work-safety/safety-topics/slips-trips-falls (accessed on 20 April 2023).
3. WHO. Falls. World Health Organization. Available online: https://www.who.int/news-room/fact-sheets/detail/falls (accessed on 24 January 2022).

4. Fong, D.T.-P.; Hong, Y.; Li, J.-X. Human walks carefully when the ground dynamic coefficient of friction drops below 0.41. *Saf. Sci.* **2009**, *47*, 1429–1433. [CrossRef]

5. Aschan, C.; Hirvonen, M.; Rajamäki, E.; Mannelin, T.; Ruotsalainen, J.; Ruuhela, R. Performance of slippery and slip-resistant footwear in different wintry weather conditions measured in situ. *Saf. Sci.* **2009**, *47*, 1195–1200.

6. Grönqvist, R.; Hirvonen, M. Slipperiness of footwear and mechanisms of walking friction on icy surfaces. *Int. J. Ind. Ergon.* **1995**, *16*, 191–200.

7. Hallas, K.; Houlihan, R.; Shaw, R.; Thorpe, S. Comparison of site-based friction measurement and slip potential. *Contemp. Ergon.* **2008**, *2008*, 723.

8. Ali, S.A.S.; Kamat, S.R. Ankle angle contribute to slip during commercial kitchen activity. *Malays. J. Med. Health Sci.* **2021**, 205–208. Available online: https://libproxy.txstate.edu/login?url=https://search.ebscohost.com/login.aspx?direct=true&db=a9h&AN=151511700&site=eds-live&scope=site (accessed on 25 April 2023).

9. Kim, J. Comparison of three different slip meters under various contaminated conditions. *Saf. Health Work.* **2012**, *3*, 22–30. [CrossRef] [PubMed]

10. Chang, W.R.; Grönqvist, R.; Leclercq, S.; Myung, R.; Makkonen, L.; Strandberg, L.; Brungraber, R.J.; Mattke, U.; Thorpe, S.C. The role of friction in the measurement of slipperiness, Part 1: Friction mechanisms and definition of test conditions. *Ergonomics* **2001**, *44*, 1217–1232. Available online: https://libproxy.txstate.edu/login?url=https://search.ebscohost.com/login.aspx?direct=true&db=edswss&AN=000173192700008&site=eds-live&scope=site (accessed on 25 April 2023). [CrossRef]

11. Kim, I.J. Practical design search for optimal floor surface finishes to prevent fall incidents. In *Accidental Falls: Risk Factors, Prevention Strategies and Long-Term Outcomes*; Nova Science Publishers, Inc.: Hauppauge, NY, USA, 2015; Chapter 5; pp. 80–103.

12. Chang, W.R.; Grönqvist, R.; Leclercq, S.; Brungraber, R.J.; Mattke, U.; Strandberg, L.; Thorpe, S.C.; Myung, R.; Makkonen, L.; Courtney, T.K. The role of friction in the measurement of slipperiness, Part 2: Survey of friction measurement devices. *Ergonomics* **2001**, *44*, 1233–1261. Available online: https://libproxy.txstate.edu/login?url=https://search.ebscohost.com/login.aspx?direct=true&db=edswss&AN=000173192700009&site=eds-live&scope=site (accessed on 20 April 2023). [CrossRef]

13. Aschan, C.; Hirvonen, M.; Mannelin, T.; Rajamäki, E. Development and validation of a novel portable slip simulator. *Appl. Ergon.* **2005**, *36*, 585–593. [CrossRef]

14. Bamberg, S.J.M.; Benbasat, A.Y.; Scarborough, D.M.; Krebs, D.E.; Paradiso, J.A. Gait Analysis Using a Shoe-Integrated Wireless Sensor System. *IEEE Trans. Inf. Technol. Biomed.* **2008**, *12*, 413–423. [CrossRef]

15. Zhu, H.; Maalej, N.; Webster, J.G.; Tompkins, W.J.; Bach-Y-Rita, P.; Wertsch, J.J. An umbilical data-acquisition system for measuring pressures between the foot and shoe. *IEEE Trans. Biomed. Eng.* **1990**, *37*, 908–911. [CrossRef]

16. Razak, A.H.A.; Zayegh, A.; Begg, R.K.; Wahab, Y. Foot plantar pressure measurement system: A Review. *Sensors* **2012**, *12*, 9884–9912. [CrossRef] [PubMed]

17. Tan, A.M.; Fuss, F.K.; Weizman, Y.; Woudstra, Y. Design of low cost smart insole for real time measurement of plantar pressure. *Procedia Technol.* **2015**, *20*, 117–122. [CrossRef]

18. Tan, A.M.; Fuss, F.K.; Weizman, Y. Development of a smart insole for medical and sports purposes. *Procedia Eng.* **2015**, *112*, 152–156. [CrossRef]

19. Anderson, W.; Choffin, Z.; Jeong, N. Empirical study on human movement classification using insole footwear sensor system and machine learning. *Sensors* **2022**, *22*, 2743. [CrossRef] [PubMed]

20. Nie, B.; Huang, R.; Yao, T.; Zhang, Y.; Miao, Y.; Liu, C.; Liu, J.; Chen, X. Textile-based wireless pressure sensor array for human-interactive sensing. *Adv. Funct. Mater.* **2019**, *29*, 180876. [CrossRef]

21. Zhang, L.; Li, H.; Lai, X.; Gao, T.; Yang, J.; Zeng, X. Thiolated graphene polyester fabric-based multilayer piezoresistive pressure sensors for detecting human motion. *ACS Appl. Mater. Interfaces* **2018**, *10*, 41784–41792. [CrossRef] [PubMed]

22. Zhu, Y.; Wu, Y.; Wang, G.; Wang, Z.; Tan, Q.; Zhao, L.; Wu, D. A flexible capacitive pressure sensor based on an electrospun polyimide nanofiber membrane. *Org. Electron.* **2020**, *84*, 105759.

23. Park, J.S.; Koo, S.-M.; Kim, C.H. Classification of standing and walking states using ground reaction forces. *Sensors* **2021**, *21*, 2145. [CrossRef]

24. Park, J.S.; Lee, C.M.; Koo, S.-M.; Kim, C.H. Gait phase detection using force sensing resistors. *IEEE Sens. J.* **2020**, *20*, 6516–6523. [CrossRef]

25. Pineda-Gutierrez, J.; Miro-Amarante, L.; Hernandez-Velazquez, M.; Sivianes-Castillo, F.; Dominguez-Morales, M. Designing a wearable device for step analyzing. In Proceedings of the 2019 IEEE 32nd International Symposium on Computer-Based Medical Systems (CBMS), Cordoba, Spain, 5–7 June 2019; IEEE: Instituto Maimónides de Investigación Biomédica de Córdoba: Cordoba, Spain, 2019; pp. 259–262.

26. Lee, S.-S.; Choi, S.T.; Choi, S.-I. Classification of gait type based on deep learning using various sensors with smart insole. *Sensors* **2019**, *19*, 1757. [CrossRef] [PubMed]

27. Djamaa, B.; Bessa, M.M.; Diaf, B.; Rouigueb, A.; Yachir, A. BoostSole: Design and realization of a smart insole for automatic human gait classification. In Proceedings of the 15th Conference on Computer Science and Information Systems (FedCSIS), Sofia, Bulgaria, 6–9 September 2020; pp. 35–43.

28. Weizman, Y.; Tan, A.M.; Fuss, F.K. Benchmarking study of the forces and centre of pressure derived from a novel smart-insole against an existing pressure measuring insole and force plate. *Measurement* **2019**, *142*, 48–59. [CrossRef]

29. Yang, C.; Lu, W.; Xia, Y. Reliability-constrained optimal attitude-vibration control for rigid-flexible coupling satellite using interval dimension-wise analysis. *Reliab. Eng. Syst. Saf.* **2023**, *237*, 109382. [CrossRef]
30. Yang, C.; Lu, W.; Xia, Y. Uncertain optimal attitude control for space power satellite based on interval Riccati equation with non-probabilistic time-dependent reliability. *Aerosp. Sci. Technol.* **2023**, *139*, 108406. [CrossRef]
31. Yang, C. An adaptive sensor placement algorithm for structural health monitoring based on multi-objective iterative optimization using weight factor updating. *Mech. Syst. Signal Process.* **2021**, *151*, 107363. [CrossRef]
32. Yang, C.; Xia, Y. A novel two-step strategy of non-probabilistic multi-objective optimization for load-dependent sensor placement with interval uncertainties. *Mech. Syst. Signal Process.* **2022**, *176*, 109173. [CrossRef]